JOURNAL OF AIRCRAFT
Vol. 34, No. 2, March–April 1997

Comparison of Computation with Experiment for a Geometrically Simplified Powered-Lift Model

Karlin R. Roth*
NASA Ames Research Center, Moffett Field, California 94035-1000

The performance of a representative short takeoff and vertical landing model during transition flight is investigated by comparison of experimental and numerical simulations. The model consists of a 60-deg cropped delta wing planform; a simple fuselage shape blended to the wing; and tandem, circular, high-pressure-air lift-jets that exit perpendicularly to the flat lower surface. The configuration minimizes the geometric complexity while retaining the important flow physics of the lift-jet/aerodynamic surface interaction. Three-dimensional, laminar, and turbulent Navier–Stokes computations are made using a multiple, overset grid scheme. Results are presented for jet-off and powered-lift cases and compared with the measured forces and pressures for the model at a freestream Mach number of 0.146, a 10-deg angle of attack, and sonic lift-jets. Computational flow visualization illustrates the presence of primary and secondary wing leading-edge vortices and the deflection of the lift-jets by the freestream. Significantly, both computational fluid dynamics and experiment predict a jet-induced lift loss that is mostly a result of a reduction in the suction pressure at the wing leading edge.

Nomenclature

b = wingspan, 27.00 in.
C_L = lift coefficient, $L/q_\infty S$
C_M = pitching moment coefficient, $M/q_\infty Sc$
C_p = pressure coefficient, $(p - p_\infty)/q_\infty$
c = wing root chord, 30.00 in.
L = lift, lb
M = pitching moment about $(x, y, z) = (c/4, 0, 0)$, ft-lb
NPR = nozzle pressure ratio, $p_{t,j}/p_j$
p = pressure, psf
q = dynamic pressure, psf
S = wing planform area, 3.19 ft^2
T = thrust, lb
x, y, z = Cartesian coordinates with origin at the model nosetip, in.
ΔL = jet-induced increment of lift, lb
ξ, η, ζ = computational coordinates

Subscripts
j = jet
t = total
∞ = freestream

Introduction

DURING the transition from hover to wingborne flight, short takeoff and vertical landing (STOVL) aircraft rely on the direct thrust of lift-jets to supplement the aerodynamic wing lift. The interaction of the lift-jets with the flow over the airframe produces a complex, three-dimensional flowfield that impacts the overall aerodynamic performance of the aircraft. More specifically, the jets usually induce a loss of lift and a change in the nose-up pitching moment on the vehicle; both effects increase with increasing forward velocity.[1,2] Thus, proper design of STOVL aircraft requires an understanding of the physics of the lift-jet/airframe interaction. The purpose of this investigation is to evaluate the ability of computational fluid dynamics (CFD) to predict the jet/airframe interaction.

The computational approach builds on experience obtained from earlier calculations of basic components of the powered-lift flowfield.[3–6] One of these component flows, the subsonic jet in crossflow, consists of a circular jet exhausting perpendicularly through a flat plate into a crossflow. The flat plate isolates the physics of the lower surface aerodynamic/propulsive interaction during transition flight. Previous Navier–Stokes simulations of the jet in crossflow show favorable quantitative agreement with experiment for the jet trajectory, the properties of the contrarotating vortex pair that dominates the jet plume, and the pressure distribution on the planar surface surrounding the jet exit.[4,5] Recent grid refinements to this model improve its performance.[6] Specifically, the refined computations capture small-scale flow features such as the horseshoe vortex system upstream of the jet and achieve improved agreement of the plate pressure distribution in the region within two diameters of the jet exit.

Two simulations extended the previous work on the numerical prediction of impinging jets to powered-lift aircraft applications. The jet-induced lift loss of a 60-deg delta wing equipped with side-by-side thrust reverser jets operating in ground effect was studied.[7,8] The simulation demonstrated the ability of the overset mesh technique to simplify the generation of body-conforming meshes, to resolve the jet flows, and to reduce computational effort without compromising solution accuracy. Smith et al.[9] modeled a complete STOVL fighter configuration, the Harrier YAV-8B, and compared the computed results with flight data. Although both simulations predicted the correct trends for the jet-induced lift loss, the lack of detailed experimental data prevented a thorough evaluation of the numerical results.

In the current research, a combined computational and experimental program provides an opportunity to critically assess the performance of the powered-lift CFD technology. The numerical simulation and the wind-tunnel test investigate the flowfield about a STOVL model whose simplified geometry minimizes the geometric modeling complexity while retaining the important flow physics of the lift-jet/aerodynamic surface interaction. In this paper, highlights of the experiment and de-

Presented as Paper 96-2431 at the AIAA 14th Applied Aerodynamics Conference, New Orleans, LA, June 17–20, 1996; received Oct. 15, 1996; accepted for publication Nov. 12, 1996.

*Aerospace Engineer, Applied Computational Aerodynamics Branch, M/S 258-1. Member AIAA.

tails of the grid generation process are presented. The jet-off computation serves as the baseline condition for the evaluation of the CFD model's ability to predict the jet-induced effects. Numerical parameters including grid resolution and turbulence modeling are examined for the jet-off conditions. Finally, computed results are compared with experimental data for the STOVL configuration with powered lift.

Wind-Tunnel Measurement Summary

The transition flight characteristics of the geometrically simplified STOVL model were measured in the NASA Ames 7- by 10-Foot Wind Tunnel. A photograph of the model installed in the test section with the wingspan oriented vertically is shown in Fig. 1. The model's cropped delta wing planform and flat lower surface are seen in the photograph. Two circular jet nozzles exit perpendicularly to the lower surface.

On the upper surface, a simple fuselage shape blends smoothly into the wing. Views of the model from the top and side are sketched in Fig. 2. The model has an overall length of 30 in., a wingspan of 27 in., a leading-edge sweep angle of 60 deg, and a trailing-edge sweep angle of −10.98 deg. The planform area for the wing is 3.19 ft^2. The radius of the rounded wing leading edge varies smoothly from 0.1 in. at the nose to 0.014 in. at the wingtip. Each of the jet nozzles has an exit diameter of 1.2 in., a length of 1.837 in., and a contraction ratio of 1.417 to 1. The jet exits are centered on the symmetry plane, $y/b = 0$. The upstream jet is located at $x/c = 0.4$, and the downstream jet is located at $x/c = 0.667$; distance is measured from the nose-tip to the center of the jet exit. Heated high-pressure air is supplied to the model plenum and ejected through the nozzles perpendicular to the wing lower surface. The model is instrumented with an internal, six-component force balance; 281 surface pressure ports; and a Kiel probe with a colocated thermocouple mounted within each nozzle. Additional details of the test apparatus and techniques are reported in Refs. 10–12.

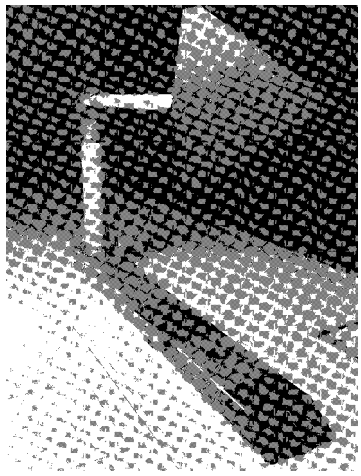

Fig. 1 Model installation with the wingspan oriented vertically in the NASA Ames 7- by 10-Foot Wind Tunnel.

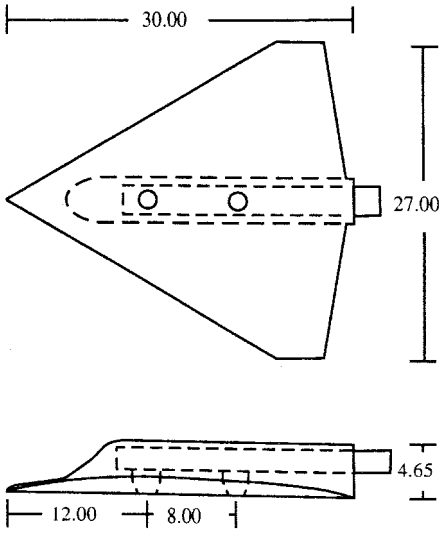

Fig. 2 STOVL model geometry. Top and side views. Dimensions are in inches.

Jet thrust, airframe aerodynamic force, and surface pressure measurements for the STOVL model were acquired over a range of angles of attack for approximately 30 combinations of freestream Mach number and jet nozzle pressure ratio (NPR). The freestream Mach number was limited to 0.2. Model angle of attack ranged from −10 to +20 deg. The nozzle pressure ratios of both jets were varied between 1–3, and the jet exit temperatures were maintained at near ambient conditions. These measurements document the effects of the effective jet velocity ratio and the model attitude on the model's aerodynamic performance.

Grid Generation

Surface Grid Definition

Surface definition data for 175 cross sections (y–z planes) were generated from the computer-aided design database. The model-based coordinate system is measured from the nosetip so that the X axis is aligned with the body, the Y axis extends spanwise with $y/b = 0$ corresponding to the symmetry plane of the model, and the Z axis indicates vertical location (see Fig. 2). The surface definition data are grouped into the five patches described in Table 1. In Table 1, the number of cross sections in each patch, the number of points defining each cross section, and the location of the starting and ending cross sections for the patch are listed. Patches 1–4 provide the majority of the wing data. A fifth patch containing the coordinates for a subset of the model fuselage was generated because the original model design was modified after the surface definition data were extracted. Within the surface definition database, a minimum cross-sectional spacing of 0.01 in. is used at the model nosetip. The maximum cross-sectional spacing is 0.5 in. on patch 2 where the geometry varies slowly. Cross sections are clustered in regions of high curvature such as the front of the fuselage or the wingtips.

The first task for the surface grid generation was to combine the fuselage geometry data with the wing data. Patch 5 was manually intersected with patches 2–4 along the side of the fuselage. Data from patch 5 were used for z values above the intersection point, and data from the wing patches were used below it. These new cross sections were used as input to the geometry preprocessor contained in PMARC, a potential-flow panel code for complex three-dimensional geometries.[13] Within the PMARC geometry package, each cross section was resplined. In addition, break points were set to delineate the fuselage–wing intersection and the wing leading-edge radius. The resplined model surface data were organized into three patches: 1) a nose patch for $x \leq 4.0$ in., 2) a main body patch, and 3) a fuselage patch for $x \geq 29.6$ in., where the fuselage extends beyond the trailing edge of the wing. These patches

Table 1 Surface definition points

Patch	Sections	Points	x start	x end
1	37	115	0.0998	5.000
2	65	175	5.000	23.000
3	46	210	23.000	27.3827
4	29	175	27.3827	30.000
5	25	100	8.800	11.500

make up the geometry database for the computational grid development.

Surface grid generation and grid topology definition were completed using the GRIDGEN codes.[14] Each of the three surface definition patches (nose, body, and fuselage) was gridded independently. Elliptic partial differential equations were solved to distribute and cluster grid points within the interior of the surface grids and to ensure that the surface grids maintain the shape of the database surfaces. The maximum grid spacing in any direction on the model surface is 10^{-2} based on the root chord.

Volume Grid Generation

Starting with the surface grid and topology information, the volume surrounding the model surface was discretized. A hyperbolic equation grid generator known as HYPGEN[15] is easy to implement, requires few computational resources, and produces smooth orthogonal grids. HYPGEN generates the three-dimensional grid by marching away from the user-input surface grid. An initial grid spacing of 10^{-5} based on root chord was used at the body surface. The body grids, which encompass the boundary layer and viscous effects near the vehicle, extend 0.08 chords or two jet diameters from the surface. The outer boundary shape is arbitrary.

Grids were also generated to resolve the wake region behind the blunt base of the fuselage and behind the wing trailing edge, which has a thickness of 0.02 in. First, copies of the final body grid plane were distributed behind the model using a hyperbolic tangent stretching function. Next, a Cartesian grid block, whose initial plane conforms to the cross-sectional shape of the rear of the fuselage, was generated algebraically using the GRIDGEN codes. Finally, a Cartesian grid block that extends from the fuselage to the wingtip was placed behind the wing to close off the trailing edge. The wind-tunnel sting mount that meets the model at the rear of the fuselage (see Fig. 1) was not simulated because it is expected to have minimal impact on wing pressures.

Grid Communication

The chimera grid scheme provides a method for oversetting three-dimensional structured grids onto a main grid.[16] Points from the main grid fall within the body boundaries of the body-fitted grids, and because the three-dimensional grids are generated somewhat independently, points from one grid may lie within the body boundary of another grid. Points that lie within the body boundary must be excluded from the computation. To accomplish this, holes are cut in the grids to accommodate the body boundaries of other grids. This creates boundaries at the edges of the holes in addition to the existing grid outer boundaries. Flow variables are passed between grids at these boundaries using trilinear interpolation. The PEGSUS code[17] is used to identify hole boundaries and to establish the interpolation stencils.

The computational domain is discretized using 10 grid blocks. The grid blocks, their descriptive names, and the number of grid points in each of the coordinate directions are listed in Table 2. The main or background grid is a relatively coarse Cartesian grid that discretizes the test section of the NASA Ames 7- by 10-Foot Wind Tunnel. Inviscid grid spacing is employed within the main tunnel grid. A second Cartesian block is embedded in the main grid to provide resolution of the viscous effects near the model. The three-dimensional body-fitted grids including the nose and body grids as well as the wake grids, which are located behind the fuselage and wing, are overset within the enriched tunnel grid. The large fuselage–wing grid block was divided into four smaller blocks to reduce computational memory requirements. Point-to-point matching is maintained at these boundaries; communication is also provided by chimera by adding one overlapped grid cell. The merged grid system utilizes 1,545,560 points to discretize one-half of the flow domain.

Table 2 Grid density for coarse grid system

Block	Grid descriptor	ξ	η	ζ
1	TUNNEL	90	36	59
2	TUNNEL2	80	51	55
3	NOSE_TIP	18	62	40
4	NOSE	21	82	40
5	BODY1	91	51	40
6	BODY2	91	61	40
7	BODY3	91	41	40
8	BODY4	47	147	40
9	FUSELAGE_REAR	39	31	60
10	WING_REAR	40	65	49

Grid Refinements

Two refinements were made to the initial grid system, which is referred to as the coarse grid. First, grid spacing on the model fuselage was rather coarse (approximately 10^{-2} streamwise and 5×10^{-3} circumferentially based on root chord) in comparison with other regions of the model. To investigate the effects of fuselage grid resolution, the number of grid points in the streamwise direction on the model fuselage (but not near the wing leading edge) was doubled for x/c between 0.133–0.400. As a result, block 5, identified in Table 2, was split into two grid zones: 1) BODY1A, $80 \times 51 \times 40$, with increased grid density and 2) BODY1B, $55 \times 51 \times 40$. This locally refined grid system is referred to as having medium density.

The overall goal of the second grid refinement was to increase grid density in flow regions dominated by viscous effects without significantly increasing the total grid size. Modifications made for the fine grid include the following:

1) Decreasing the spacing in the streamwise direction at the nosetip from 3.3×10^{-4} to 8.3×10^{-5}, based on root chord.

2) Increasing the number of streamwise grid points for x/c between 0.133–0.45 by a factor of approximately 1.8 about the entire body.

3) Decreasing the number of circumferential points on the fuselage from 29 to 22.

4) Increasing the number of circumferential points near the wing leading edge.

5) Extending the body grids an additional 0.08 chords further from the body surface in the normal direction.

6) Increasing the boundary-layer grid spacing at the body surface to $z/c = 2.5 \times 10^{-5}$.

7) Increasing streamwise grid spacing in the wake grids.

The resulting overset mesh contains 1.9 million points for jet-off computations; grid zones are described in Table 3.

Jet Grids

For powered-lift simulations, two jet grids are added to the overset mesh. The symmetry plane of the fine grid system, including the jet grids, is shown in Fig. 3. Each jet grid is a polar grid with a constant radius of 2.5 jet diameters that extends five jet diameters away from the body surface. The grids are clustered in the radial direction near the jet exit with 25 points within the jet exit in the radial direction, a spacing of nearly 0.07 jet diameters at the axis and a minimum spacing

Table 3 Grid density for fine grid system

Block	Grid descriptor	ξ	η	ζ
1	TUNNEL	90	36	59
2	TUNNEL2	80	51	55
3	NOSE_TIP	25	67	50
4	BODY1	180	95	50
5	BODY2	180	50	50
6	FUSELAGE_REAR	19	31	60
7	WING_REAR	23	40	31
8	JET1	50	37	60
9	JET2	50	37	60

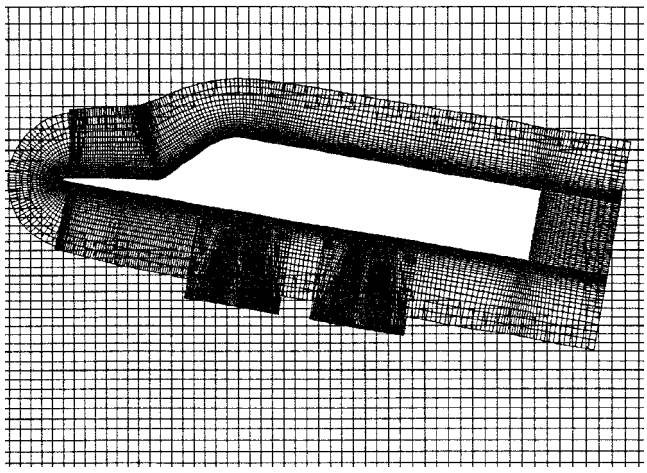

Fig. 3 Merged grid system in the symmetry plane.

of approximately 0.006 jet diameters at the edge of the exit. The radial clustering is relaxed in grid planes located farther from the jet exit. The normal grid spacing at the jet exit matches the boundary-layer spacing employed in the body grids near the solid surface. The maximum spacing in the normal direction is approximately 0.4 jet diameters.

Computational Method

Numerical Algorithm

The OVERFLOW code[18] used for these calculations is a multiple zone, multischeme, Navier–Stokes flow solver. The numerical method selected for the computations is an implicit, three-factor, diagonalized, central-difference scheme for a thin-layer formulation of the Reynolds-averaged Navier–Stokes equations.[19,20] Thin-layer viscous terms are retained in all three coordinate directions. The algorithm is first-order in time, second-order in space, and uses second- and fourth-order ARC3D-type numerical dissipation. The second-order dissipation parameter is set to zero for all computations. The fourth-order dissipation, DIS4, is initially set to 0.02 and then reduced to 0.01.

Explicit Boundary Conditions

For the STOVL model simulation, the following explicit boundary conditions are applied. The model surface is a viscous adiabatic solid wall. The nosetip grid has a C–O topology necessitating an axis condition on the nosetip. Both jets are modeled using a constant velocity profile with sonic, ambient temperature flow at the exits. Experimental measurements indicate that the flow is nearly symmetric. Therefore, to reduce the computational resource requirements for these nontime accurate computations, a plane of symmetry is imposed at $y/b = 0$. The wind-tunnel walls are modeled using an inviscid adiabatic wall condition. At the upstream boundary of the tunnel, density and the three components of momentum are set to freestream, and pressure is extrapolated from the interior of the flowfield. Downstream pressure is held constant while the other flow variables are extrapolated.

Turbulence Modeling

Turbulence modeling for powered-lift flowfields is difficult. Simple algebraic models fail to represent the flow physics, particularly in the wakes of the lift-jets. Unfortunately, one-equation models such as the Baldwin–Barth turbulence transport equation[21] have not demonstrated better results than the algebraic models.[6] Although two-equation models may more accurately characterize the flow physics for powered-lift flowfields, solution of the additional transport equations and the small time steps needed for the turbulent solution make this approach impractical for a complete aircraft. Therefore, the turbulence modeling philosophy adopted for this study is to resolve the body surface boundary layers with an algebraic model, realizing that the jet-plume turbulence is neglected and that jet-wake turbulence may not be adequately modeled, and to evaluate the impact of this assumption.

The Baldwin–Lomax turbulence model[22] performs satisfactorily for simple configurations that have regions of mild separation and reattachment. The model computes an algebraic length scale based on the vorticity distribution for the boundary layer. Because solution of the algebraic equation set provides an eddy viscosity for only a small increase in computational memory and time, it has been modified and extended to complex flows. For flows with crossflow separation such as the delta wing where there are distinct layers of vorticity, the Baldwin–Lomax model may be unable to correctly identify an appropriate length scale. A modification to the model developed by Degani and Schiff[23] terminates the search for a length scale once it is established that the maximum in the boundary layer close to the body surface has been found. The Degani and Schiff modification[23] has been employed effectively in previous simulations (e.g., Refs. 24 and 25) of rounded and sharp leading-edge delta wings and has been used for the turbulent simulations presented in this paper.

Conventional Wingborne Flight Results

For the power-off simulations, the model has a 10-deg angle of attack and 0-deg yaw. The freestream Mach number is 0.146; at this condition a reasonable convergence rate can be obtained for the compressible flow solver. The freestream Reynolds number, based on the root chord length, is 2.52×10^6. For conventional wingborne flight, suction pressure peaks are located on the upper surface of the wing for angles of attack greater than 5 deg; the locations move to the wing's lower surface at angles less than 0 deg. Thus, for simulations at $\alpha = 10$ deg, wing vortices are established on the upper surface of the wing away from the lower surface jet interaction region.

The computations are made using Cray Y-MP and Cray C90 computers. A steady-state solution is obtained using a spatially varying time step. Convergence is determined by monitoring the L_2 norm of the residual and the lift coefficient for each of the computational grids. Convergence rates are affected by the slow development of the flow behind the fuselage and in the jet plumes. Steady-state solutions are obtained in approximately 8000 steps without power and in approximately 10,000 steps with powered lift. The turbulent, coarse grid, jet-off computations require approximately 11 million words of memory and 10 s of CPU time per iteration on the Cray C90.

Grid Refinements

To evaluate grid effects, turbulent solutions computed using the coarse, medium, and fine overset grid systems are compared with the measured surface pressure distribution. Figure 4 presents pressure data for the upper surface of the model along the symmetry plane. A series of spanwise pressure coefficient plots for the upper and lower surfaces at stations $x/c = 0.267$, 0.400, 0.533, 0.667, and 0.800 is presented in Fig. 5. These locations correspond to the pressure tap locations on the

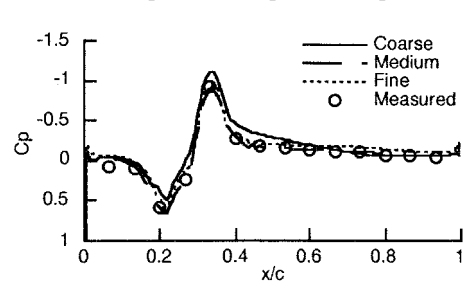

Fig. 4 Effects of grid refinement on surface pressures in the symmetry plane for turbulent jet-off computations.

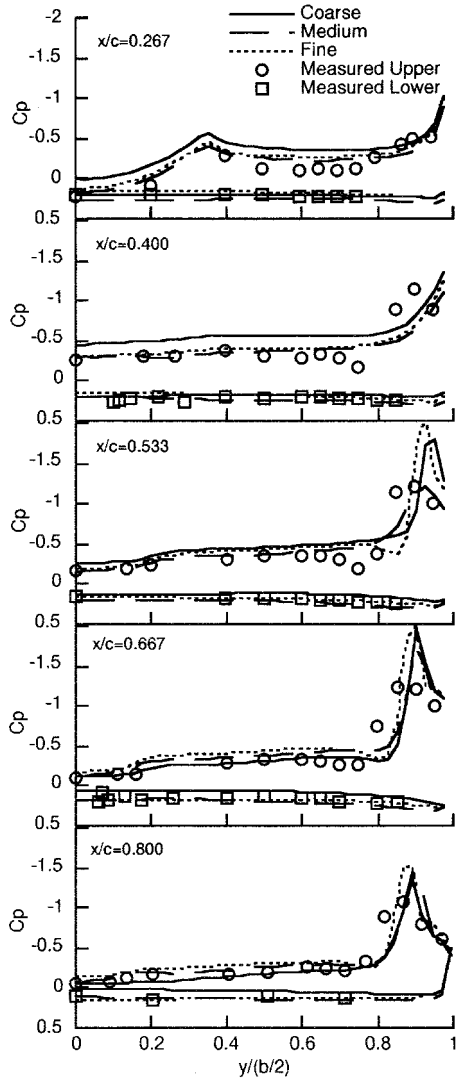

Fig. 5 Effects of grid refinement on spanwise pressure distribution for turbulent jet-off computations.

wind-tunnel model. It should be noted that the surface pressure plots at constant chordwise locations were constructed by interpolating data from the computational solutions at 40 evenly spaced spanwise locations with increments of $y/(b/2) = 0.025$.

The freestream flow approaches the model and stagnates on the lower surface, close to the nosetip (Fig. 4). On the upper surface, the predicted surface pressures are lower than the measurements for $x/c < 0.133$. Decreasing the streamwise grid spacing at the nosetip (fine grid) fails to improve the agreement.

Coarse grid computations on the forward half of the model ($x/c < 0.5$) predict pressures that are lower than experiment both near the fuselage and across most of the wing (Fig. 5). In contrast, the medium grid results, which have the most grid refinement on the fuselage in the region between $x/c = 0.133$–0.400, provide the best agreement with experiment on the forward portion of the wing and fuselage. This demonstrates the importance of resolving the flow near the model fuselage for this configuration.

Although none of the solutions demonstrate good agreement near the wing leading edge, some observations are made. First, at $x/c = 0.267$, where the flowfield is dominated by the presence of the model fuselage, increasing the streamwise grid density near the wing leading edge (fine grid) does not make a significant impact. Next, pressure suction peaks at the downstream stations, $x/c > 0.400$ are nearly the same in location and magnitude for the coarse and medium grid computations; grid density in this region is identical for these simulations. Finally, for the fine grid solution, which places additional grid points near the wing leading edge, the pressure suction peak moves slightly inboard at all stations.

During conventional wingborne flight, the pressures on the flat lower wing surface are nearly equal to the freestream static pressure as shown in Fig. 5 for all of the computations. The scatter in the experimental data near $y/b = 0$ at both $x/c = 0.400$ and 0.667 is because of the presence of the jet exit openings. These openings are not modeled in the computation.

Turbulence Model Effects

As shown in Fig. 6, using fine grid results, both laminar and turbulent computations predict low pressures in the symmetry plane upstream of $x/c = 0.133$. In both cases, the locations of the high-pressure peak on the front of the fuselage and the low-pressure peak as the flow moves over the top of the fuselage are predicted. Similarly, all computed solutions agree well with the measured data on the model's lower surface as demonstrated in the spanwise pressure distributions at $x/c = 0.400$ and 0.667, shown in Fig. 7.

One difference between the laminar and turbulent solutions is the prediction of flow separation near the model fuselage. A small region of reversed flow is predicted as the geometry curves from the nose to the fuselage (see Figs. 2 and 6). In the symmetry plane, $y/b = 0$, this reversed flow region is smaller for the turbulent computations, extending from $x/c = 0.19$ to 0.21, than for the laminar prediction that shows reversed flow between $x/c = 0.17$–0.20. The turbulent separation region is confined to a very small region near the symmetry plane, whereas the laminar solution shows a horseshoe vortex wrapped around the base of the model fuselage. The laminar calculation also shows a second separation as the flow moves over the top of the fuselage between $x/c = 0.37$–0.40. In con-

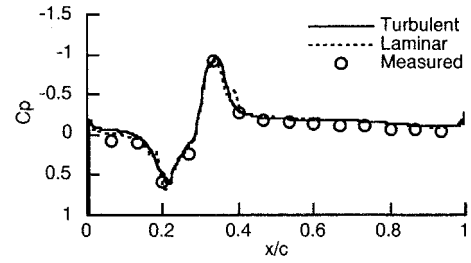

Fig. 6 Effects of turbulence model on surface pressures in the symmetry plane for jet-off solutions computed on the fine grid.

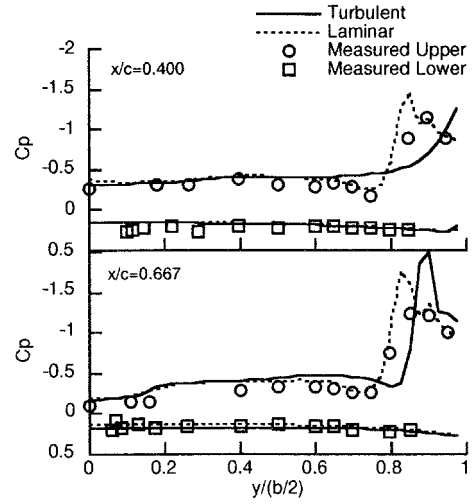

Fig. 7 Effects of turbulence model on spanwise pressure distribution for jet-off solutions computed on the fine grid.

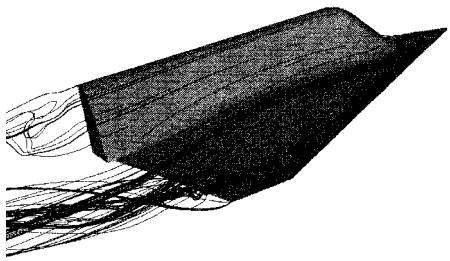

Fig. 8 Computed particle traces for conventional flight.

trast, the turbulent flow remains attached. Relatively sparse pressure measurements near the model fuselage cannot verify the predicted reversed-flow regions.

At the forwardmost station, $x/c = 0.267$, the laminar solution, like the turbulent solutions, does not match the magnitudes of the measured pressure distribution across most of the span. However, near the wing leading edge and aft of $x/c = 0.267$, it more closely resembles the measured pressure distribution on the upper surface of the wing (Fig. 7). At the wing leading edge, the pressure suction peaks for the laminar calculation are initiated further inboard, cover more wing area, and have slightly less suction than the turbulent flow prediction.

Computational Flow Visualization

Particle traces for the computed turbulent flow are presented in Fig. 8. The particles are released within the boundary layer at several stations along the body. The primary separation line, which is the location where the vorticity sheet leaves the surface to form the primary vortex, begins at the nosetip and extends along the leading edge of the wing moving slightly outboard near the wingtips. Since the leading-edge radius of the model decreases from the nose to the wingtip, the separation location is probably affected by the nearly sharp-edged geometry near the wingtip. The formation of the secondary separation line is delayed until approximately $x/c = 0.4$. These surface flow patterns are illustrated in Ref. 26. Qualitatively, the simulation captures key elements of the vortex-dominated leading-edge flow that is typical for delta wings at moderate to high angles of attack.

Power Effects

For the jet-on simulations, laminar and turbulent computations were made using the fine grid with the model at an angle of attack of 10 deg, a freestream Mach number of 0.146, and sonic lift-jets. This corresponds to a nozzle pressure ratio of 1.9 and an effective velocity ratio, $(q_\infty/q_j)^{0.5}$, of 0.145 for the lift-jets. These jet conditions are somewhat different from the experimental data[10–12] used for comparison. In the experiment, to maintain sonic conditions for the front jet, the rear jet is underexpanded with NPR = 2.0. This corresponds to a measured total thrust of 45.88 lb for the lift-jets with 56.9% of the thrust supplied by the rear jet, whereas the simulated jets each deliver 23 lb of thrust. Also, as shown in Ref. 10, the total pressure varies across the jet exits. It is expected that the top hat velocity profile with sonic jet exit boundary conditions will be sufficient for initial comparisons; however, for more detailed analysis, the experimental exit profiles should be modeled.

Lift Characteristics

The FOMOCO utilities[27] are used to calculate forces and moments on the overset grid systems. The FOMOCO procedure produces a single hybrid grid consisting of nonoverlapping quadrilaterals connected by a triangulated mesh and integrates the forces and moments on the hybrid grid. For the jet-off cases, $C_L = 0.443$, 0.487, 0.519, and 0.511 for the coarse, medium, and fine grid turbulent cases and the fine grid laminar case, respectively, whereas the measured value is $C_L = 0.477$. Less agreement is achieved for pitching moment. Coarse grid computations show an increase in nose-up moment, and fine grid computations show an increase in nose-down moment compared with the measured nose-down moment, $C_M = -0.159$; at best, $C_M = -0.171$ using the medium grid.

To evaluate power effects, the difference between power-on and power-off lift is computed. The measured jet-induced lift loss is $\Delta L/T = -0.398$, which is equivalent to nearly a 4-deg reduction in angle of attack. Significantly, the computations also show a lift loss because of the lift-jets: $\Delta L/T = -0.26$ (laminar) and $\Delta L/T = -0.36$ (turbulent). While the global features of the jet-induced lift loss are captured, the surface pressure distribution for the powered lift cases will be used to highlight local variations between the computations and measurements.

Wing Leading-Edge Flow

Some similarities exist for the laminar and turbulent jet-on cases and the experiment. First, no significant variation in the symmetry plane surface pressure distribution is obtained for the powered-lift conditions vs unpowered conditions for either the experiment or the computations. Also, at the forwardmost station, $x/c = 0.267$, there is little difference between the laminar and turbulent predictions and there is practically no influence from the lift-jets. Finally, examining Fig. 7 (jet-off) and Fig. 9a (jet-on) shows that the lift-jets reduce the magnitude of the leading-edge suction pressures at most stations.

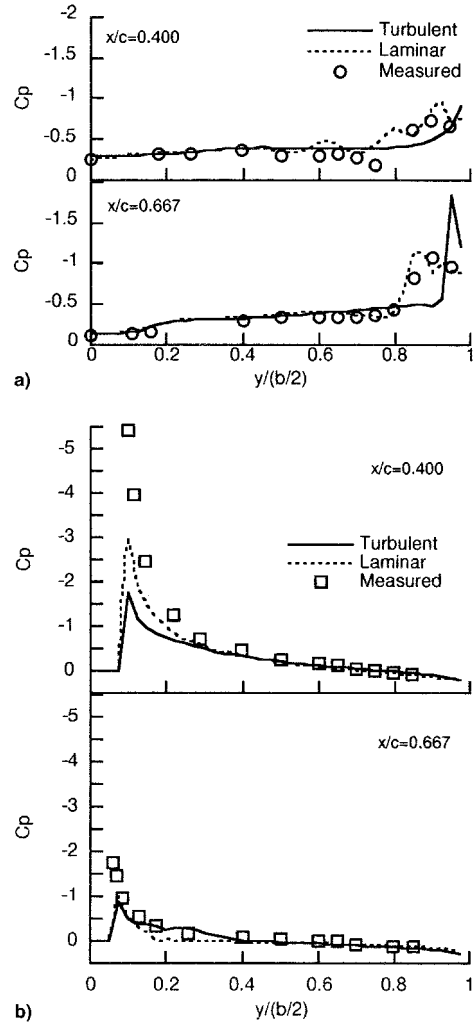

Fig. 9 Surface pressure distribution for laminar and turbulent jet-on computations: a) upper and b) lower surfaces.

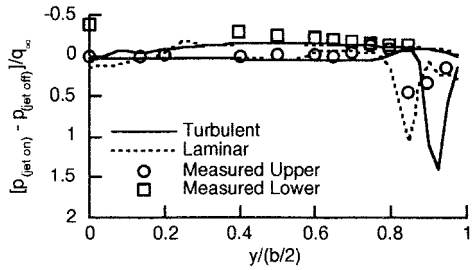

Fig. 10 Jet-induced increment of pressure coefficient at x/c = 0.533.

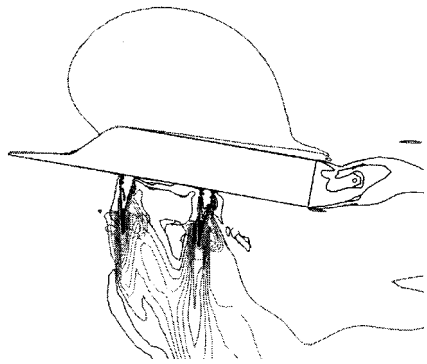

Fig. 11 Mach contours in the symmetry plane with lift-jets.

In Fig. 9, the computed surface pressures are compared with experimental data at two stations, x/c = 0.400 and 0.667; these locations correspond to the origins of the lift-jets. For clarity, the pressures on the model upper and lower surfaces are plotted on separate figures. As shown in the jet-off computations, the pressure suction peak near the wing leading edge on the model upper surface tends to have greater suction and to be closer to the leading edge for the turbulent computation, whereas the laminar solution tends to show better agreement with the measured pressures at the leading edge.

The jet-induced increment of pressure coefficient, plotted in Fig. 10 for x/c = 0.533, is determined by subtracting the power-off pressures from the power-on pressures. On the upper surface of the wing, positive values indicate a jet-induced lift loss at the wing leading edge. The jet-induced increment of pressure on the outboard portion of the wing lower surface is close in magnitude to the measurements and shows an increase in lift with the jets. However, in the region near the symmetry plane that physically lies in the wake of the front jet, the powered-lift flowfield is not adequately modeled.

Jet Flow

Mach number contours within the symmetry plane illustrate the jet flows (Fig. 11). The contours show the structure of the flowfield as the front jet exits into the freestream flow and how its plume is deflected. The aft jet penetrates further into the flow before deflecting because it is shielded from the freestream by the front jet. This behavior parallels experimental flow visualization.[10,11] Close inspection of the contours indicates that there is some numerical dissipation at the interface between the finer jet grids and the outer flow grid (TUNNEL2).

The lift-jets induce low pressures on those areas of the lower surface of the wing that are close to the jet exits. However, as shown in Fig. 9b, the simulated pressure distribution near the jets does not provide as much lift as the measured pressure distribution. The failure to predict the low pressures in the vicinity of the jet exit is similar to the results for a single jet in crossflow presented in Ref. 6.

Concluding Remarks

Three-dimensional, laminar, and turbulent Navier–Stokes computations of a geometrically simplified STOVL model configured for conventional wingborne flight and powered-lift operations are reported. Computational flow visualization shows the structure of the wing leading-edge vortices and the deflection of the lift-jets. Computations made using grid refinements, particularly near the model fuselage and wing leading edge, provide better agreement with the measured surface pressure distribution. Neither the laminar nor the turbulent computations completely characterize the wing leading-edge flowfield or the flow within two diameters of the jet exits. For laminar calculations, the pressure suction peaks at the wing leading edge tend to be initiated further inboard, cover more area on the wing, have slightly less suction, and agree better with the measurements than the turbulent predictions. The simulations predict a jet-induced lift loss for the model that is mostly because of decreased suction at the wing leading edge. Low pressures near the sides and in the wakes of the lift-jets are not adequately simulated. Additional study of the jet grid structure and application of the measured conditions at the jet exits are recommended.

References

[1]Margason, R. J., and Fearn, R. L., "Jet-Wake Characteristics and Their Induced Aerodynamic Effects on V/STOL Aircraft," NASA SP-218, Sept. 1969.

[2]Kuhn, R. E., and Stewart, V. R., "Lift and Pitching Moment Induced on Jet STOVL Aircraft Hovering in Ground Effect — Data Report," U.S. Air Force Wright Lab., TR-93-3044, June 1993.

[3]Van Dalsem, W. R., "Study of Jet in Ground Effect with a Crossflow Using the Fortified Navier-Stokes Scheme," AIAA Paper 87-2279, Aug. 1987.

[4]Roth, K. R., Fearn, R. L., and Thakur, S. S., "Evaluation of a Navier-Stokes Prediction of a Jet in a Crossflow," *Journal of Aircraft*, Vol. 29, No. 2, 1992, pp. 185–193.

[5]Roth, K. R., "Influence of the Thin-Layer Approximation on Jet in Crossflow Computations," AIAA Paper 90-3056, Aug. 1990.

[6]Chiu, S., Roth, K. R., Margason, R. J., and Tso, J., "A Numerical Investigation on a Subsonic Jet in Crossflow," AGARD 72nd Fluid Dynamics Panel Meeting and Symposium on Computational and Experimental Assessment of Jets in Cross Flow, Winchester, England, UK, April 1993 (Paper 22).

[7]Chawla, K., and Van Dalsem, W. R., "Numerical Simulation of a Powered-Lift Landing," AGARD 72nd Fluid Dynamics Panel Meeting and Symposium on Computational and Experimental Assessment of Jets in Cross Flow, Winchester, England, UK, April 1993 (Paper 32).

[8]Chawla, K., Van Dalsem, W. R., and Rao, K. V., "Simulation of a Delta Wing with Two Jets in Ground Effect," *Computing Systems in Engineering*, Vol. 1, Nos. 2–4, 1990, pp. 483–494.

[9]Smith, M. H., Chawla, K., and Van Dalsem, W. R., "Numerical Simulation of a Complete STOVL Aircraft in Ground Effect," AIAA Paper 93-4880, Dec. 1993.

[10]Roth, K. R., "A Powered Lift Experiment for CFD Validation," AIAA Paper 91-1731, June 1991.

[11]Roth, K. R., "Transitional Flight Characteristics of a Geometrically Simplified STOVL Model," AGARD 72nd Fluid Dynamics Panel Meeting and Symposium on Computational and Experimental Assessment of Jets in Cross Flow, Winchester, England, UK, April 1993 (Paper 34).

[12]Roth, K. R., "STOVL CFD Validation Test Case," *A Selection of Experimental Test Cases for the Validation of CFD Codes*, AGARD-AR-303, Vols. I and II, Aug. 1994.

[13]Ashby, D. L., Dudley, M. R., Iguchi, S. K., Browne, L., and Katz, J., "Potential Flow Theory and Operation Guide for the Panel Code PMARC," NASA TM 102851, Jan. 1991.

[14]Steinbrenner, J. P., Chawner, J. R., and Fouts, C. L., "The GRIDGEN 3D Multiple Block Grid Generation System," Vols. I and II, Wright Research and Development Center, TR-3022, Wright–Patterson AFB, OH, July 1990.

[15]Chan, W. M., and Steger, J. L., "A Generalized Scheme for Three-Dimensional Hyperbolic Grid Generation," AIAA Paper 91-1586, June 1991.

[16]Benek, J. A., Buning, P. G., and Steger, J. L., "A 3-D Chimera

Grid Embedding Technique," AIAA Paper 85-1523, July 1985.
[17]Tramel, R. W., and Suhs, N. E., "PEGSUS 4.0 User's Manual," Arnold Engineering and Development Center, TR-91-8, June 1991.
[18]Renze, K. J., Buning, P. G., and Rajagopalan, R. G., "A Comparative Study of Turbulence Models for Overset Grids," AIAA Paper 92-0437, Jan. 1992.
[19]Pulliam, T. H., and Chaussee, D. S., "A Diagonal Form of an Implicit Approximate Factorization Algorithm," *Journal of Computational Physics*, Vol. 39, No. 2, 1981, p. 347.
[20]Beam, R. M., and Warming, R. F., "An Implicit Factored Scheme for the Compressible Navier-Stokes Equations," *AIAA Journal*, Vol. 16, No. 4, 1978, pp. 393–402.
[21]Baldwin, B. S., and Barth, T. J., "A One-Equation Turbulence Transport Model for High Reynolds Number Wall-Bounded Flows," AIAA Paper 91-0610, Jan. 1991.
[22]Baldwin, B. S., and Lomax, H., "Thin-Layer Approximation and Algebraic Model for Separated Turbulent Flows," AIAA Paper 78-0257, Jan. 1978.
[23]Degani, D., and Schiff, L. B., "Computation of Supersonic Viscous Flows Around Pointed Bodies at Large Incidence," AIAA Paper 83-0034, Jan. 1983.
[24]Craig, K. J., "Computational Study of the Aerodynamics and Control by Blowing of Asymmetric Vortical Flows over Delta Wings," Ph.D. Dissertation, Stanford Univ., Stanford, CA, Aug. 1992.
[25]Ekaterinaris, J. A., and Schiff, L. B., "Numerical Simulation of the Effects of Variation of Angle of Attack and Sweep Angle on Vortex Breakdown over Delta Wings," AIAA Paper 90-3000, Aug. 1990.
[26]Roth, K. R., "An Initial Comparison of CFD with Experiment for a Geometrically Simplified STOVL Model," AIAA Paper 93-3059, July 1993.
[27]Chan, W. M., and Buning, P. G., "Zipper Grids for Force and Moment Computation on Overset Grids," AIAA Paper 95-1681, June 1995.